MID-INFRARED PROPERTIES AND COLOR SELECTION FOR X-RAY-DETECTED ACTIVE GALACTIC NUCLEI IN THE MUSYC EXTENDED CHANDRA DEEP FIELD–SOUTH

Carolin N. Cardamone,[1,2] C. Megan Urry,[1,2] Maaike Damen,[3] Pieter van Dokkum,[1,2] Ezequiel Treister,[4] Ivo Labbé,[5] Shanil N. Virani,[1,2] Paulina Lira,[6] and Eric Gawiser[7]

ABSTRACT

We present the mid-infrared colors of X-ray-detected AGNs and explore mid-infrared selection criteria. Using a statistical matching technique, the likelihood ratio, over 900 IRAC counterparts were identified with a new MUSYC X-ray source catalog that includes ~1000 published X-ray sources in the Chandra Deep Field–South and Extended Chandra Deep Field–South. Most X-ray-selected AGNs have IRAC spectral shapes consistent with power-law slopes, $f_\nu \propto \nu^\alpha$, and display a wide range of colors, $-2 \leq \alpha \leq 2$. Although X-ray sources typically fit to redder (more negative α) power laws than non-X-ray-detected galaxies, more than 50% do have flat or blue (galaxy-like) spectral shapes in the observed 3–8 μm band. Only a quarter of the X-ray-selected AGNs detected at 24 μm are well fit by featureless red power laws in the observed 3.6–24 μm, likely the subset of our sample whose infrared spectra are dominated by emission from the central AGN region. Most IRAC color selection criteria fail to identify the majority of X-ray-selected AGNs, finding only the more luminous AGNs, the majority of which have broad emission lines. In deep surveys, these color selection criteria select 10%–20% of the entire galaxy population and miss many moderate-luminosity AGNs.

Subject headings: infrared: galaxies — quasars: general — X-rays: galaxies

1. INTRODUCTION

Theoretical arguments and observational evidence indicate that active galactic nuclei (AGNs) may play an important role in galaxy evolution (Fabian et al. 2003, 2006; Croton et al. 2006; Kriek et al. 2007; Sijacki et al. 2007; Schawinski et al. 2007). The study of this mutual feedback requires a complete sample of AGNs, their host galaxies, and comparable inactive galaxies at the same epochs. To discover these populations, surveys with deep multiwavelength coverage are necessary.

Today, AGNs are identified at many wavelengths, each of which selects a slightly different sample. For example, radio surveys preferentially find radio-loud AGNs (Brinkmann et al. 2000), while optical and ultraviolet-excess surveys find luminous unobscured AGNs (Richards et al. 2004; Mazzarella & Balzano 1986). Because they detect all but the most heavily obscured AGNs, hard X-ray surveys efficiently select relatively unbiased and complete samples of AGNs (Brandt & Hasinger 2005), even if X-ray background models predict a still-hidden population of Compton-thick AGNs (Treister et al. 2004; Worsley et al. 2005). For obscured AGNs (roughly three-fourths of the total population), the rest-frame optical light is dominated by the host galaxy (e.g., Treister et al. 2004; Treister & Urry 2006). This obscuring gas and dust eventually reemits the absorbed X-rays at infrared wavelengths. In general, the optical/infrared spectral shapes of AGNs contain two broad components of thermal emission: the "big blue bump" seen at optical and ultraviolet wavelengths, often attributed to emission from a hot accretion disk and visible only in unobscured AGNs, and an infrared excess attributed to reradiation from circumnuclear dust on larger scales visible in all AGNs in the far-infrared (Sanders et al. 1989; Sanders 1999; Pier & Krolik 1992).

Mid-infrared diagnostic studies have found strong continuum emission originating in dust heated by the intense nuclear radiation field, an important indicator of AGN emission (Laurent et al. 2000). Indeed, surveys with the *Spitzer Space Telescope* Infrared Array Camera (IRAC; Fazio et al. 2004) are finding AGNs via color selection techniques by targeting strong red power-law continua (Alonso-Herrero et al. 2006; Hickox et al. 2007; Donley et al. 2007). This emission can be used to find even Compton-thick AGNs (Polletta et al. 2006). However, many color selection techniques developed with *Spitzer* data have been based on the infrared colors of optically selected AGN samples in shallow surveys (e.g., Lacy et al. 2004; Stern et al. 2005; Hatziminaoglou et al. 2005). The ideal AGN selection technique is both highly reliable, meaning most objects selected are indeed AGNs, and highly complete, meaning most AGNs are identified. To evaluate and improve infrared selection of AGNs, it is important to investigate how the mid-infrared colors of X-ray-selected AGN samples compare to those of optically selected samples.

Finding high-redshift AGNs in multiwavelength surveys requires both a large area and sensitive detection limits. The Multiwavelength Survey by Yale-Chile (MUSYC;[8] Gawiser et al. 2006) is a square-degree survey of four fields to limiting depths of $R_{AB} = 26$ and $K_{AB} = 22$ ($K_{AB} = 23$ in the central areas; Quadri et al. 2007) with extensive follow-up spectroscopy. One MUSYC field, the Extended Chandra Deep Field–South (ECDF-S), has been surveyed by the *Chandra X-Ray Observatory* (Giacconi et al. 2002, hereafter G02; Alexander et al. 2003, hereafter A03; Lehmer

[1] Department of Astronomy, Yale University, New Haven, CT 06511.
[2] Yale Center for Astronomy and Astrophysics, Yale University, P.O. Box 208121, New Haven, CT 06520.
[3] Leiden Observatory, Universiteit Leiden, 2300 RA Leiden, Netherlands.
[4] European Southern Observatory, Santiago, Chile.
[5] Carnegie Observatories, Pasadena, CA 91101.
[6] Departamento de Astronomía, Universidad de Chile, Casilla 36-D, Santiago, Chile.
[7] Department of Physics and Astronomy, Rutgers University, Piscataway,

et al. 2005, hereafter L05; Virani et al. 2006, hereafter V06). The sensitivity of the *Chandra* data allows for detection of luminous AGNs out to large redshifts[9] and more modest luminosity AGNs ($\sim 10^{42}$–10^{44} ergs s^{-1}) back to the quasar era ($z \sim 2$; Brandt & Hasinger 2005). Recently, the existing MUSYC data in the ECDF-S were augmented with very deep IRAC *Spitzer* data in the SIMPLE[10] survey (M. Damen et al. 2008, in preparation) and by GOODS and the *Spitzer* Wide-area InfraRed Extragalactic survey (SWIRE) at 24 μm (Dickinson et al. 2003; Lonsdale et al. 2003). These two surveys are among the deepest *Spitzer* observations. This results in a large sample of X-ray-selected AGNs with mid-infrared coverage, unique in the combination of area and X-ray and infrared depth.

In this paper we evaluate mid-infrared selection techniques using the X-ray-selected sample of AGNs in the ECDF-S. In § 2 we describe the X-ray and infrared data, detail the likelihood ratio–matching technique used to find *Spitzer* counterparts for each X-ray source, and present the infrared identifications. We investigate the mid-infrared colors of these X-ray sources in § 3. In § 4 we compare our sources to published IRAC selection criteria and assess the impact of adding the 24 μm data to the IRAC bands. In § 5 we discuss why the majority of our X-ray-selected AGNs would be missed by current infrared selection criteria. Conclusions are given in § 6. Throughout this paper we assume $H_0 = 71$ km s^{-1} Mpc^{-1}, $\Omega_m = 0.3$, and $\Omega_\lambda = 0.7$.

2. OBSERVATIONS AND ANALYSIS

2.1. *Chandra Data*

Three X-ray surveys have overlapping coverage of the same region of the sky: the very deep central Chandra Deep Field–South (CDF-S; G02; A03), the deep ECDF-S (L05; V06), and the shallower *XMM-Newton* pointing that covers this region (Streblyanska et al. 2004). For this study, we use only the two *Chandra* surveys because the higher resolution of *Chandra* allows for fainter point-source detections. In contrast, the *XMM-Newton* data are better suited for X-ray spectroscopy of the brighter sources because of the larger effective area (Streblyanska et al. 2006; Dwelly & Page 2006). The CDF-S consists of 1 Ms of data reaching a limiting on-axis flux of 5.2×10^{-17} ergs s^{-1} cm^{-2} (2.8×10^{-16} ergs s^{-1} cm^{-2}) in the 0.5–2.0 keV (2.0–8.0 keV) band (A03). The 11 individual pointings of the CDF-S cover a central area of $\sim$300 arcmin^2 (G02). The four 250 ks *Chandra* pointings of the ECDF-S overlap the deep central region, covering a total area of $\sim$1100 arcmin^2. On axis the ECDF-S reaches a limiting flux of 1.7×10^{-16} ergs s^{-1} cm^{-2} (3.9×10^{-16} ergs s^{-1} cm^{-2}) in the 0.5–2.0 keV (2.0–8.0 keV) band (V06). We combine published point-source detections from these fields into a new unified MUSYC X-ray point-source catalog.

We begin with the most conservative detection catalogs for the CDF-S and ECDF-S, A03 and V06. Since the CDF-S goes significantly deeper in flux than the ECDF-S and covers a much smaller area between the four ECDF-S pointings, we expect that only a fraction of sources will be common to both surveys. Both catalogs use similar detection methodologies: first filtering the data to eliminate periods of high X-ray background, then using `wavdetect` (Freeman et al. 2002) for source selection, which is robust in detecting individual sources in crowded fields. The MUSYC X-ray catalog first adopts the 326 sources presented in Table 3 of A03. We next search for new sources in Tables 4 and 5 of V06, as described in what follows. Table 4, the primary catalog in V06, uses the same conservative false-positive probability threshold for detection ($p_{\rm thresh} = 10^{-7}$) as A03. Given this detection threshold, we expect no more than two or three false X-ray sources in either A03 or Table 4 of V06. Table 5 of V06, with $p_{\rm thresh} = 10^{-6}$, allows for a larger percentage of false positives but includes a greater number of bona fide X-ray sources in the catalog that would otherwise be missed. In order to improve the absolute astrometric solutions in the V06 catalogs, small shifts were applied to the X-ray sources' right ascension and declination, $\leq 1''$. The shifts were calculated for each of the four pointings in the ECDF-S using optical counterparts in the MUSYC *BVR* image. No shift was necessary to align the A03 catalog positions. For each source in V06, we calculated the distance to the nearest X-ray sources in A03 and defined combined X-ray positional uncertainties for each pair by $\sigma = (\sigma_{\rm A03}^2 + \sigma_{\rm V06}^2)^{1/2}$, where $\sigma_{\rm XR}$ is the 1 σ error of a Gaussian based on the positional errors reported in each catalog. We included in our MUSYC X-ray catalog the 503 sources from V06 that were more than 4 σ ($\sim 3''$) from any source in A03. The choice of 4 σ is conservative and was determined by detailed inspections of both the X-ray and MUSYC *BVR* images. The median separation between the reported source positions for the 148 X-ray sources found in both A03 and V06 was $0.58''$. A total of 829 unique X-ray sources resulted from the union of A03 and V06, the first 771 of which were detected with the conservative false-positive probability threshold.

We next investigated the other published X-ray catalogs in this field for the same two data sets. L05 created a larger source catalog for the ECDF-S region by retaining data obtained during small X-ray background flares and using the same lower significance threshold parameter as Table 5 in V06. A very small, $\leq 1''$, positional shift was applied to the L05 catalog to align the astrometry to the MUSYC *BVR* image. Using the X-ray positional uncertainties, we found 141 additional X-ray sources in L05. Finally, G02 used a set of unique detection methods, including a modified version of SExtractor (Bertin & Arnouts 1996) and running `wavdetect` with different selection criteria. Three catalogs are presented in G02: their Table 2 contains sources common to both detection methods, Table 3 contains SExtractor sources only, and Table 4 contains `wavdetect` sources only. A slightly larger fixed positional shift ($\sim 1''$) was necessary to align the X-ray sources presented in G02 with our MUSYC *BVR* image. Using X-ray positional uncertainties, we found a total of 47 additional X-ray sources in G02 not previously presented in A03, V06, or L05: 17 from Table 2, 19 from Table 3, and 10 from Table 4. Although there is a good possibility that some of these additional X-ray sources may be spurious, those will fail to match to an infrared counterpart and thus do not affect the conclusions of this paper (see § 2.3).

The complete MUSYC X-ray catalog contains 1017 individual sources whose X-ray properties are given in columns (1)–(5) in Table 1. Column (1) presents a new unique MUSYC X-ray ID number for each source. Column (2) presents the original X-ray catalog and catalog ID for each X-ray source (e.g., V06:323 is source number 323 from V06). All X-ray source properties, such as flux or count rate, are taken from the referenced detection catalog. Columns (3) and (4) present the right ascension and declination (J2000.0) for each X-ray source, based on the MUSYC *BVR* image. They are on a common system incorporating the small Δright ascension and Δdeclination applied to each catalog to shift the coordinates to agree with the MUSYC *BVR* image. Column (5) gives the hardness ratio, defined by $(H - S)/(H + S)$, where H and S are the X-ray counts in the hard (2–8 keV) and soft (0.5–2 keV) bands, respectively. For sources detected only

[9] Luminous AGNs ($L_{\rm X} \sim 10^{44}$ ergs s^{-1}) can, in principle, be detected to very high redshifts in the ECDF-S ($z \sim 10$), but the volume sampled is too small to make such a detection likely.

[10] See http://www.astro.yale.edu/dokkum/SIMPLE/.

TABLE 1

X-Ray and Infrared Properties of MUSYC ECDF-S X-Ray Sources

ID (1)	Cat. ID[a] (2)	R.A. (J2000.0) (3)	Decl. (J2000.0) (4)	HR[b] (5)	3.6 μm[c] (μJy) (6)	4.5 μm[c] (μJy) (7)	5.8 μm[c] (μJy) (8)	8.0 μm[c] (μJy) (9)	24.0 μm[d] (μJy) (10)	L_X[e] (ergs s^{-1}) (11)	Notes[f] (12)
1.....	A03:1	52.934208	−27.823917	−0.09	1.52 (0.14)	1.89 (0.15)	1.62 (0.62)	2.31 (0.57)	... (...)	...	
2.....	A03:2	52.936333	−27.865639	−0.43	6.69 (0.12)	7.94 (0.14)	5.33 (0.56)	5.98 (0.57)	... (...)	...	
3.....	A03:3	52.936875	−27.860889	−0.24	11.95 (0.13)	14.31 (0.15)	17.28 (0.56)	14.77 (0.58)	... (...)	...	
4.....	A03:4	52.947083	−27.887028	−0.34	15.15 (0.13)	22.73 (0.14)	32.26 (0.58)	46.54 (0.54)	... (...)	...	
5.....	A03:5	52.949917	−27.845972	−0.54	5.48 (0.14)	4.25 (0.16)	3.93 (0.61)	2.71 (0.62)	... (...)	43.53	2 BL
6.....	A03:6	52.950083	−27.800528	−0.47	23.38 (0.13)	28.93 (0.15)	30.18 (0.62)	22.41 (0.60)	S: 560.34 (28.32)	41.37	5
7.....	A03:7	52.955958	−27.776222	−0.37	13.32 (0.13)	16.04 (0.16)	20.63 (0.59)	25.57 (0.63)	... (...)	44.17	5
8.....	A03:8	52.956208	−27.842778	−0.28	5.33 (0.14)	7.03 (0.16)	7.80 (0.61)	7.44 (0.62)	... (...)	...	
9.....	A03:9	52.959958	−27.845028	0.10	15.81 (0.14)	19.24 (0.15)	15.07 (0.61)	10.65 (0.62)	... (...)	...	
10.....	A03:10	52.960125	−27.864389	−0.42	12.34 (0.12)	11.83 (0.15)	8.86 (0.57)	7.60 (0.58)	... (...)	...	
11.....	A03:11	52.961000	−27.883583	−0.33	2.42 (0.13)	2.85 (0.15)	2.54 (0.59)	6.24 (0.59)	... (...)	...	
12.....	A03:12	52.963167	−27.847667	−0.29	25.68 (0.14)	16.94 (0.16)	13.30 (0.60)	8.44 (0.62)	... (...)	42.57	2 non-BL

Notes.—Units of right ascension and declination are degrees. Table 1 is published in its entirety in the electronic edition of the *Astrophysical Journal*. A portion is shown here for guidance regarding its form and content.

[a] Original detection catalog for X-ray source and X-ray source ID therein. Counts and flux are taken from this catalog.

[b] Hardness ratio, defined by $(H - S)/(H + S)$, where H and S are the X-ray counts in the hard (2–8 keV) and soft (0.5–2 keV) bands, respectively. For sources detected only in the hard band (soft band), the hardness ratio is set equal to 1 (−1). For sources detected only in the full band (0.5–8 keV), the hardness ratio is set equal to 10. G02 defined the hard band as 2–10 keV. Therefore, we adjusted the published hard-band counts from G02 to equal those that would have been detected at 2–8 keV, the hard band defined by the other three authors, using PIMMS (ver. 3.9c; Mukai 1993) with the average X-ray spectrum measured by G02.

[c] Infrared flux in μJy followed by 1 σ error in parentheses, from the SIMPLE survey (M. Damen et al. 2008, in preparation).

[d] 24 μm flux in μJy followed by 1 σ error in parentheses. Source of 24 μm flux is indicated by S for SWIRE (Lonsdale et al. 2003) or G for GOODS (Dickinson et al. 2003).

[e] Observed luminosity in ergs per second in the 0.5–8 keV band, using references given in col. (12).

[f] Source of redshift used to calculate the luminosity: 0 for VLT FORS2 spectroscopy, ver. 1.0; 1 for VIMOS VLT Deep Survey, ver. 1.0; 2 for spectroscopic redshifts from Szokoly et al. (2004); 3 for spectroscopic redshifts from Croom et al. (2001); 4 for spectroscopic redshifts determined from MUSYC spectroscopy (E. Treister et al. 2008, in preparation); and 5 for photometric redshifts from COMBO-17 (Wolf et al. 2004). Where known, spectra showing broad emission lines (BL) are distinguished from those without broad lines (non-BL).

in the hard band (soft band), the hardness ratio is set equal to 1 (−1). For sources detected only in the full band (0.5–8 keV), the hardness ratio is set equal to 10. G02 defined the hard band as 2–10 keV. Therefore, we adjusted the published hard-band counts from G02 to equal those that would have been detected at 2–8 keV, the hard band defined by the other three authors, using PIMMS (ver. 3.9c; Mukai 1993) with the average X-ray spectrum measured by G02 ($\Gamma = 1.4$; $H_{2-8} = 0.9896 H_{2-10}$).

2.2. *Spitzer Data*

Considerable *Spitzer* time has been invested in the ECDF-S with both IRAC and the Multi-Band Imaging Photometer for *Spitzer* (MIPS; Rieke et al. 2004). GOODS, along with additional Guaranteed Time Observer (GTO) time, gathered deep IRAC and MIPS data on the central region of this field (Dickinson et al. 2003). In addition, SWIRE (Lonsdale et al. 2003) covers a nearly 8 deg^2 region around the original CDF-S in a shallow survey mode with both MIPS and IRAC. Finally, a public deep IRAC survey was conducted in the region covering the ECDF-S (SIMPLE; PI: P. van Dokkum).

The IRAC data cover 3–8 μm to 5 σ limiting depths of 24.4 (3.6 μm), 24.0 (4.5 μm), 22.2 (5.8 μm), and 22.2 (8.0 μm) in AB magnitude. In units of flux density, these values are 0.63, 0.91, 4.7, and 4.7 μJy, respectively. A catalog of more than 60,000 sources was created with SExtractor using a weighted sum of the 3.6 and 4.5 μm data (M. Damen et al. 2008, in preparation). Of these, we have reliable photometry in all four IRAC bands for 38,755 sources (3 σ), which will be used in this study. The astrometry was calibrated using the MUSYC *BVR* detection image ($R_{AB} = 27.1$); the resulting positional accuracy for individual sources is $\lesssim 0.3''$ (1 σ; M. Damen et al. 2008, in preparation).

We also use the SWIRE 24 μm catalog provided in Data Release 3 (Lonsdale et al. 2003; Surace et al. 2005), which covers the entire area of the X-ray data to AB magnitude 18 (0.23 mJy), and the GOODS data in the central region, which goes ∼5 mag deeper (Dickinson et al. 2003). We adopt the aperture fluxes from the SWIRE catalog which agree with the published GOODS fluxes to better than 5%. The positional accuracy of the 24 μm data is considerably less than that of the IRAC data; however, all 24 μm source positions were matched to IRAC sources, decreasing the positional uncertainties.

2.3. *Catalog Matching*

Following the work of Brusa et al. (2005, 2007), we use the likelihood ratio, a statistical matching technique, to find *Spitzer* counterparts to the ECDF-S X-ray sources. Although the median positional accuracy of *Chandra* is ∼0.6″, off-axis the PSF broadens and becomes circularly asymmetric, leading to larger positional uncertainties in faint off-axis sources. The positional accuracy for each detected *Chandra* source depends on the number of counts detected and the distance of the source from the aim point. For several X-ray sources, this positional uncertainty encompasses multiple potential infrared counterparts, while for others there may be no counterpart to the survey detection limits. Due to the high source density of the faintest IRAC sources, there is a non-negligible random chance of finding a faint IRAC object near an unassociated X-ray source. Simulations showed that ∼60% of random positions in the field fall within 4″ of an IRAC source, the maximum distance for which we find an IRAC counterpart for an X-ray source. The likelihood ratio takes into account the background object density and the positional accuracy of both the *Spitzer* and the *Chandra* data and returns the probability that

a given match is the correct one. A nearest neighbor approach, restricted to a typical search radius of 1.5″, would miss 109 IRAC counterparts that we recover with our technique. Although larger search radii can return more possible counterparts, a nearest neighbor approach does not indicate which counterparts fall inside the search area by chance, and it can only distinguish among multiple possible candidates by their distance from the reported X-ray source position. Our method weights the distance using the positional errors and adds a prior on the brightness of the prospective counterpart.

The likelihood ratio is the ratio between the probability of finding the true infrared counterpart at a given distance from a particular X-ray source divided by the probability of finding a background object at that distance (see Sutherland & Saunders 1992; Ciliegi et al. 2003). When matching the ith X-ray source to a possible jth infrared counterpart, we calculate

$$LR_{ij} = \frac{q(m_j) f(r_{ij})}{n(m_j)}, \tag{1}$$

where $q(m)$ is our empirically determined probability distribution for infrared counterparts as a function of magnitude, $f(r)$ is the probability distribution function of the positional errors in source i and counterpart j [modeled as a two-dimensional Gaussian defined by $\sigma_{\rm Gaussian} = (\sigma^2_{{\rm X},i} + \sigma^2_{{\rm IR},j})^{1/2}$], and $n(m)$ is the surface density of background objects as a function of magnitude. When calculating the probability distribution function of the positional errors, $\sigma_{{\rm X},i}$ is unique to each X-ray source depending on its off-axis angle and brightness, while no such field-dependent distinction is made for the infrared counterparts. We adopt $\sigma_{\rm IRAC} = 0.3''$ and $\sigma_{24\,\mu{\rm m}} = 0.5''$ (§ 2.2). Both $q(m)$ and $n(m)$ depend on the depth of the infrared data. This technique is inherently Bayesian, and the resulting likelihood ratio assumes that the priors $q(m)$, $n(m)$, and $f(r)$ are known.

When calculating the background counts of infrared sources, $n(m)$, we correct for the fact that there are actually fewer faint sources near X-ray objects than near random positions in the field (Brusa et al. 2007). This follows from the high probability of finding a bright infrared counterpart near any given X-ray position and the fact that the fainter sources very close to these bright counterparts go undetected. To do this we first estimate the background around a sample of IRAC objects with a magnitude distribution similar to those IRAC objects located within 1″ of the X-ray source positions; the positional uncertainties make it highly probable that IRAC objects within this distance are true counterparts. Subtracting this estimated background magnitude distribution from the magnitude distribution of the actual IRAC sources near the X-ray source positions provides a better estimate of the magnitude distribution of IRAC sources associated with X-ray sources. Experimentation shows that using this improved estimate is stable to multiple iterations. We then estimate the background around a sample of IRAC sources with this final magnitude distribution for objects associated with X-ray source positions; this is the $n(m)$ used in our likelihood ratio calculations.

Next, we count the total number of infrared objects lying within a distance r of all X-ray sources, $N_{\rm total}(m)$. Then we multiply the background distribution by the area searched to find these sources; the latter is the number of X-ray sources, $N_{\rm X}$, times the area of each circle searched, πr^2. The difference between $N_{\rm total}(m)$ and the expected background, $n(m) N_{\rm X} \pi r^2$, is our expected distribution of real counterparts, $N_{\rm real}(m)$. It is important to understand that this is a statistical quantity; rather than predicting the expected infrared counterpart for any individual X-ray source, it calculates the expected magnitude distribution for all $N_{\rm X}$ sources. With our expected distribution of real counterparts we derive the normalization, Q, as the ratio of the total expected number of real counterparts, $\sum N_{\rm real}(m)$, divided by the total number of X-ray sources, $N_{\rm X}$. Then we compute our expected distribution of true infrared counterparts as a function of magnitude,

$$q(m) = \frac{N_{\rm real}(m)}{\sum_m N_{\rm real}(m)} Q. \tag{2}$$

Finally, we compute the likelihood ratio for each infrared object located near an X-ray source using equation (1).

When we search for infrared counterparts over a larger radius, we see more possible counterparts, but the large distance between these prospective counterparts and the X-ray source drives down the likelihood ratio. We must then carefully select the best likelihood ratio which can distinguish between true matches and false matches. Because the presence of multiple prospective counterparts provides additional knowledge of the likelihood ratio, we use the reliability (R) to select counterparts (Sutherland & Saunders 1992). The reliability is the probability that a given infrared counterpart is the correct infrared counterpart for each X-ray source. For each possible infrared counterpart j, we calculate the reliability by

$$R = \frac{LR_j}{\sum LR_i + (1 - Q)}. \tag{3}$$

Here $\sum LR_i$ is the sum over all possible infrared counterparts for a given X-ray source. The $(1 - Q)$ term is the probability of there being no infrared counterpart. The calculated reliabilities form a bimodal distribution, clustering at values above $R = 0.9$ and below $R = 0.1$, and dividing cleanly at $R = 0.6$. Therefore, we accept all matches with $R \geq 0.6$. The likelihood ratio approach assumes exact knowledge of the priors, $q(m)$ and $n(m)$. Because we estimate these values from the data, the likelihood ratio does not reflect uncertainties in our estimation of the background. However, with a threshold value of $R = 0.6$, we find from Monte Carlo simulations of the background estimation that fewer than 1% of our matches are affected by this uncertainty.

2.4. *Spitzer* Counterparts

We find that more X-ray sources in the ECDF-S are detected with *Spitzer* than at any other wavelength. For the full MUSYC X-ray catalog of 1017 sources, we find 921 *Spitzer* counterparts in the IRAC data, a 90% recovery rate. Of the 921 sources, 908 have 3 σ detections in all four of the IRAC channels. For many of the X-ray sources, blending and confusion of IRAC sources, sometimes due to proximity to a very bright source, are responsible for the lack of IRAC counterparts. Excluding regions where confusion or bright stars interfere, we recover infrared counterparts for 98% of the high-confidence X-ray source detections, i.e., the subset of the X-ray sources detected in the ECDF-S with the conservative false-probability threshold. For the remaining 2% of X-ray sources, either an IRAC source is seen on the image near the X-ray position but is not above the source detection limit of the IRAC catalog (two cases), or between two and five IRAC sources are located at larger distances from the X-ray position (2″–4″) and no single source has a large enough probability of being the correct counterpart (14 cases). We find no convincing case of an undetected high-significance X-ray source in the IRAC image. That is, essentially all X-ray sources in our catalog are bright enough in the infrared to be detected in the deep IRAC data.

There are 453 unique MIPS counterparts combining the results from the 24 μm surveys in this field. We find 181 X-ray counterparts in the SWIRE catalog and 318 counterparts in the GOODS catalog from the central region. Combining the counterparts found in the MIPS and IRAC data, we have 428 sources with complete spectral energy distributions (SEDs) from 3.0 to 24 μm.

All matched counterparts and their mid-infrared fluxes are presented in Table 1. Columns (6), (7), (8), and (9) give the observed flux in the 3.6, 4.5, 5.8, and 8.0 μm IRAC bands, respectively. The flux units are in μJy and are followed by the 1 σ errors in parentheses. Column (10) gives the MIPS 24 μm flux in μJy followed by the 1 σ error in parentheses. The number is preceded by a G if it comes from the deeper GOODS data and an S if it is taken from the shallower SWIRE.

2.5. *Redshifts*

Although the majority of X-ray sources turn out to be AGNs, it is also possible for deep X-ray surveys to detect Galactic stars, as well as galaxies that are vigorously forming stars. Luminosities above 10^{42} ergs s^{-1} separate out sources that are primarily powered by black hole accretion rather than star formation (Persic et al. 2004; Lira et al. 2002). In order to study intrinsic X-ray luminosities and to apply a luminosity cut to exclude Galactic stars and starburst galaxies from our AGN sample, we require some knowledge of a source's distance or redshift. To this end, we are obtaining optical spectra of our X-ray-detected sources using Magellan IMACS and VLT VIMOS (E. Treister et al. 2008, in preparation). Thus far, we have 281 spectra for our X-ray sample, 110 with secure redshifts and 113 with spectral-type identifications: 42 broad-line sources (BLAGNs), 47 non-broad-line luminous ($\log L_X \geq 42$ ergs s^{-1}) X-ray sources (non-BLAGNs), 15 galaxies ($\log L_X \leq 42$ ergs s^{-1}) showing no AGN features in their spectra, and 9 stars (E. Treister et al. 2008, in preparation). The BLAGNs are typically referred to as type 1 AGNs, while sources showing narrow lines are referred to as type 2 AGNs. However, these spectral signatures are often hidden in obscured and moderate-luminosity AGNs with large host galaxies (Moran et al. 2002; Severgnini et al. 2003). Therefore, we define non-BLAGNs to be all sources showing narrow emission lines suggestive of type 2 AGN emission plus those sources with $\log L_X \geq 42$ ergs s^{-1} that show galaxy-like optical spectra. To the 110 redshifts we obtained with IMACS, we add an additional 173 sources with spectroscopic redshifts published in the literature (Szokoly et al. 2004; Croom et al. 2001; Le Fèvre et al. 2004; Vanzella et al. 2005). We further include spectroscopic identifications from Szokoly et al. (2004), which add 33 BLAGNs and 74 non-BLAGNs. Another 274 sources have high-quality photometric redshifts from the COMBO-17 survey (Wolf et al. 2004). We note that our sample of AGNs spans a range of $L_X(0.5\text{–}8\ \mathrm{keV}) \sim 10^{42}\text{–}10^{45}$ ergs s^{-1}, typical for deep X-ray surveys and different from the shallower survey sources, which are on average more luminous. This makes a total of 557 X-ray sources (60% of the counterpart sample) for which we can calculate the X-ray luminosity in the observed 0.5–8 keV band: of these, 416 (76%) have $L_X(0.5\text{–}8\ \mathrm{keV}) \geq 10^{42}$ ergs s^{-1} and thus are bona fide AGNs.

In Table 1 we present the X-ray luminosities and spectral identifications. Column (11) gives the observed 0.5–8 keV luminosity calculated from the redshift. For sources from G02, no 0.5–8 keV flux was reported. Therefore, we adjusted the published 2–10 keV counts from G02 to equal those that would have been detected at 0.5–8 keV, using PIMMS (ver. 3.9c; Mukai 1993) with the average X-ray spectrum measured by G02 ($\Gamma = 1.4$; $F_{0.5\text{–}8} = 1.13F_{2\text{–}10}$). Column (12) gives the source of the redshift estimate used to calculate the X-ray luminosity as follows: 0 for VLT FORS2 spectroscopy, version 1.0; 1 for VIMOS VLT Deep Survey, version 1.0; 2 for Szokoly et al. (2004); 3 for Croom et al. (2001); 4 for redshifts determined from the MUSYC spectroscopy (E. Treister et al. 2008, in preparation); and 5 for COMBO-17 (Wolf et al. 2004). Those counterparts falling into the categories of BLAGNs and non-BLAGNs are also indicated.

3. THE MID-INFRARED COLORS OF X-RAY SOURCES

From 3.6 to 8.0 μm X-ray-detected sources show a wide range of colors. In Figure 1, a color-color plot of the infrared counterparts to the MUSYC X-ray catalog, sources with blue colors are in the lower left region and those with red colors are located in the upper right. A linear relation extends from blue to red along a track occupied by power-law SED shapes ($f_\nu \sim \nu^\alpha$). Along this track, asterisks indicate α-values of +1.5 (*lower left*) to -1.5 (*upper right*) in steps of 0.5. For each source, X-ray luminosities are indicated where known: $L_X \geq 10^{42}$ ergs s^{-1} plotted with light blue crosses, $L_X \leq 10^{42}$ ergs s^{-1} plotted with green dashes, and those with unknown redshifts plotted with black plus signs. It is clear that the X-ray-selected AGNs, $L_X \geq 10^{42}$ ergs s^{-1}, extend along the full range of power-law shapes. We also explore the infrared colors of the X-ray counterparts identified as BLAGNs (*dark blue square*s) and non-BLAGNs (*red circles*). For comparison, we plot the mean type 1 quasar SED compiled by Richards et al. (2006), from redshift 0 to 6 (*dot-dashed purple line, counterclockwise*). Unsurprisingly, the BLAGNs lie near the type 1 quasar track and have the reddest infrared colors. Still, many AGNs have significantly bluer colors than the type 1 track, falling down and to the left in Figure 1. In contrast, the sources classified as non-BLAGNs are roughly evenly split between red ($\alpha \leq 0$) and blue ($\alpha \geq 0$) colors. Overall, while the optically identified BLAGNs tend to have the reddest infrared colors, the X-ray-selected AGN population is *not all* red in color.

Next, we compare the IRAC colors of the X-ray sources (908) to the ~40,000 IRAC sources showing no X-ray emission to the limits of the published X-ray surveys, most of which are inactive galaxies. In Figure 2 we display two popular IRAC color-color plots; the outlined regions in the right and left panels correspond to two different proposed selection techniques (§ 4), and the contours enclose 75%, 50%, 25%, and 15% of the IRAC sources. The left panel shows $\log (S_{5.8})/(S_{3.6})$ versus $\log (S_8)/(S_{4.5})$, where S is the observed flux in μJy, and on the right we plot Vega magnitudes, $[5.8] - [8.0]$ versus $[3.6] - [4.5]$. For clarity we plot only $L_X \geq 10^{42}$ ergs s^{-1} sources and indicate only the BLAGNs. In both panels, the power-law SED track and type 1 QSO SED track are repeated from Figure 1. Although a larger percentage of the AGNs have red colors than the galaxies, in neither plot are the X-ray-selected AGNs clearly separated from the rest of the galaxies.

Because the galaxies and AGNs appear to lie along the locus of power laws, we fit the four observed IRAC fluxes, 3.6–8.0 μm, to power-law SEDs. Within the short baseline of IRAC, nearly all of our sources are consistent with power laws, especially given the photometric uncertainties. Each source with detections in all four IRAC channels was fit by $f_\nu \propto \nu^\alpha$; 94% of all sources and 97% of the X-ray-selected AGNs had acceptable fits by power laws (χ^2, $p \geq 0.05$). In Figure 3 we compare the histogram of the power-law indices, α, for the X-ray-selected AGNs and other sources. Both types of sources show a very broad range in α, but the AGNs tend to be slightly redder than normal galaxies (more negative α). A K-S test rejects the hypothesis that the two distributions come from the same population ($P = 0.0014$). While only 17% of the

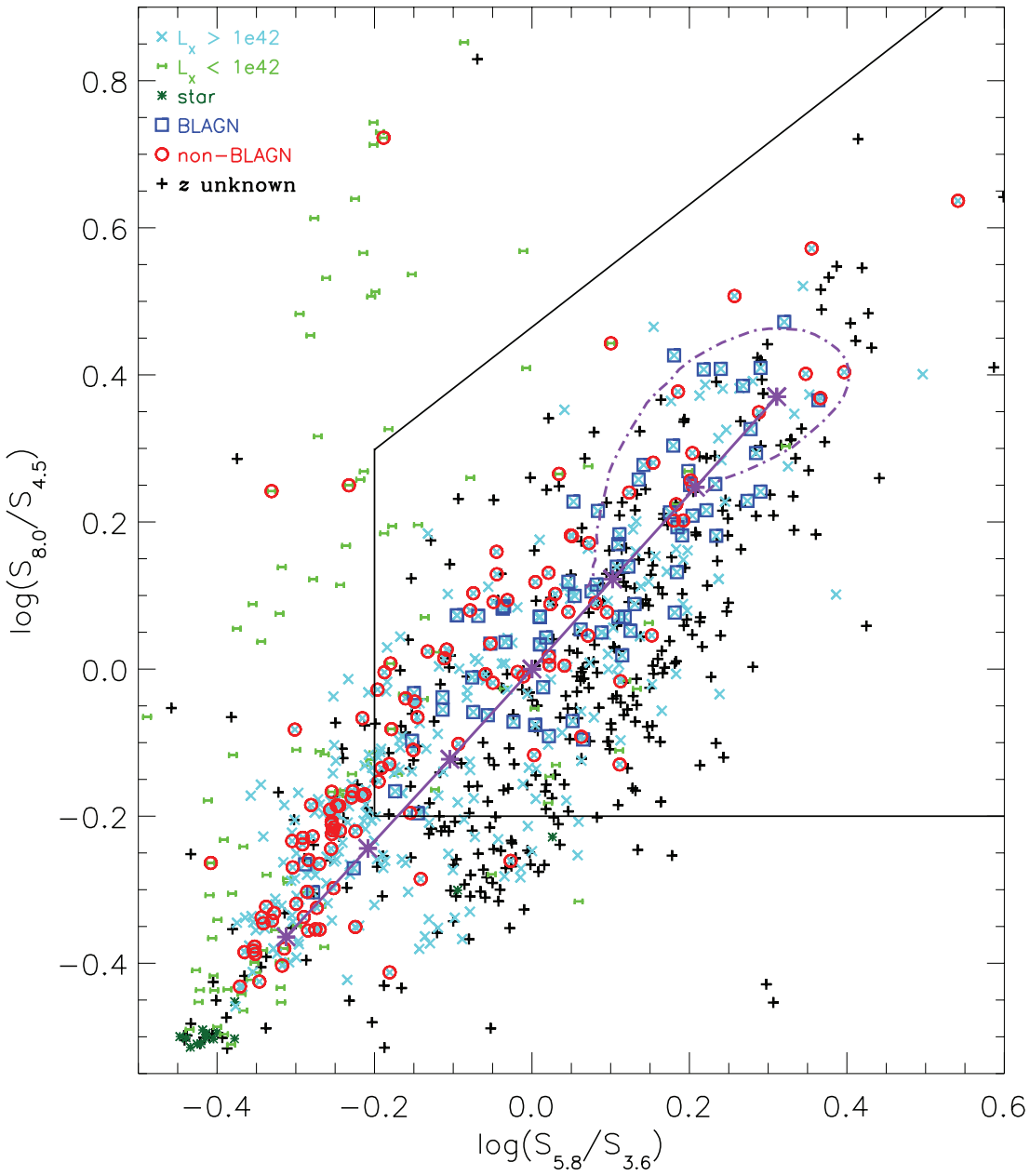

FIG. 1.—Color-color plot for the MUSYC X-ray sources. Also shown are two SED tracks: (1) the mean type 1 quasar SED from Richards et al. (2006) redshifted from $z = 0$ to 6 (*dot-dashed purple line, counterclockwise*) and (2) the pure power-law SEDs, $f_\nu \propto \nu^\alpha$ (*solid purple line*), with asterisks marking power-law exponents of $\alpha = +1.5$ to -1.5 (*bottom left to top right*, $\Delta\alpha = 0.5$). X-ray-selected AGNs (*light blue crosses*) have colors consistent with power-law SEDs from the bluest to reddest colors shown here. The black lines indicate the region suggested by Lacy et al. (2004) for selecting AGNs, which excludes 42% of X-ray-selected AGNs ($L_X \geq 10^{42}$ ergs s^{-1}).

galaxy sample has $\alpha \leq 0$, 37% of $L_X \geq 10^{42}$ ergs s^{-1} sources fit a negative power law. Optically selected AGN spectra show red continuum emission at infrared wavelengths, with $\alpha \sim -1$ (e.g., Elvis et al. 1994). This is consistent with our finding that 100% of the BLAGNs have acceptable power-law fits, 72% with $\alpha \leq 0$ (*cross-hatched histogram*). As a whole, our power-law fits to the BLAGNs are consistent with featureless negative power-law slopes in the mid-infrared. However, we find a broad range of α-values even for the BLAGNs. Similarly, the non-X-ray-detected galaxies are bluer as a whole than the AGN population, even considering that the sources with the reddest α in the X-ray-selected AGN histogram may be broad-line objects. Indeed, although the X-ray-selected AGNs have on average slightly more negative α-values than galaxies, over half (59%) of X-ray-selected AGNs are fit by power laws with positive exponents similar to those of the bulk of the galaxy population. Therefore, we find that most X-ray-selected AGNs do not show red continuum emission at observed *Spitzer* IRAC wavelengths.

4. SELECTING AGNs BY INFRARED COLORS

Although selecting AGNs through X-ray emission is relatively unbiased, current X-ray surveys may still be missing AGNs that are heavily obscured by large columns of dust and gas. All AGNs, whether obscured or unobscured at optical wavelengths, reprocess and reemit the absorbed radiation in the mid- and far-infrared (Granato & Danese 1994; Nenkova et al. 2002). Because AGNs are expected to be luminous at infrared wavelengths, several authors have developed infrared selection techniques for AGNs

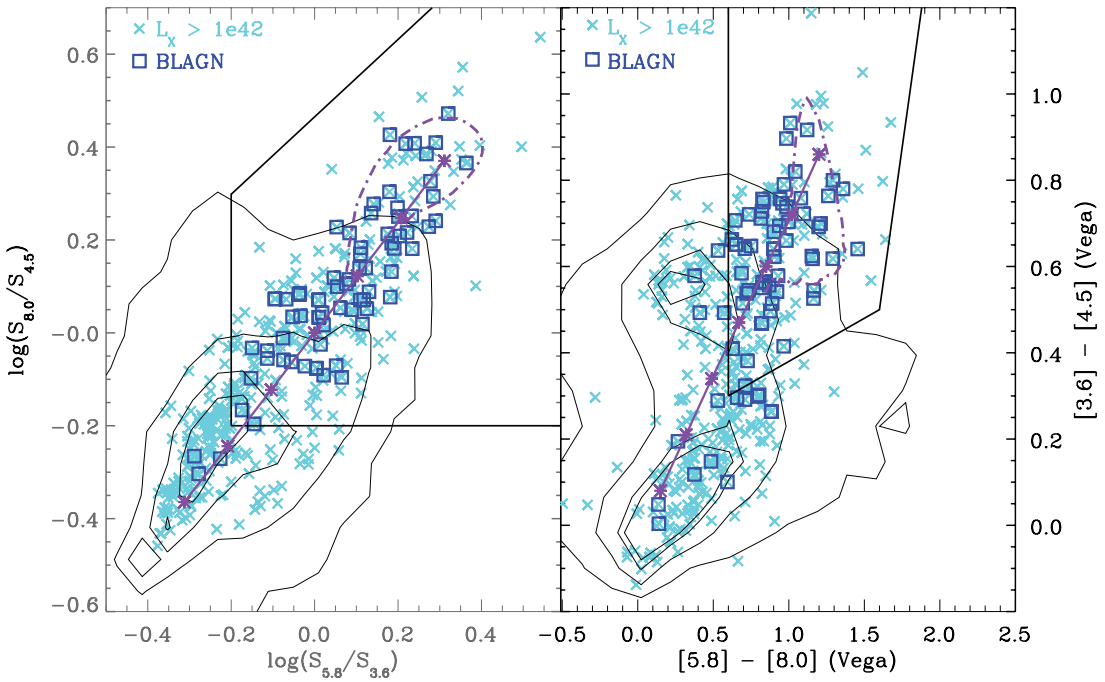

FIG. 2.—Color-color plots for all sources in the MUSYC catalog (contours indicate 75%, 50%, 25%, and 15% of the IRAC sources). The non-X-ray-detected galaxies and X-ray-selected AGNs are not well separated in this color space. *Left*: Region defined by Lacy et al. (2004) includes nearly 20% of all IRAC-detected galaxies. Therefore, this selection region is not effective at identifying a sample of AGNs. *Right*: Selection box of Stern et al. (2005) uses a different color-color plot of the IRAC bands. Only ~40% of X-ray-selected AGNs ($L_X \geq 10^{42}$ ergs s^{-1}) fall into this region. Because it eliminates 90% of the general population of MUSYC sources, this selection box is more effective at indicating potential AGNs but misses a larger fraction of the X-ray-selected AGNs. X-ray-selected AGNs occupy a far larger region in mid-infrared color space than optically selected BLAGNs.

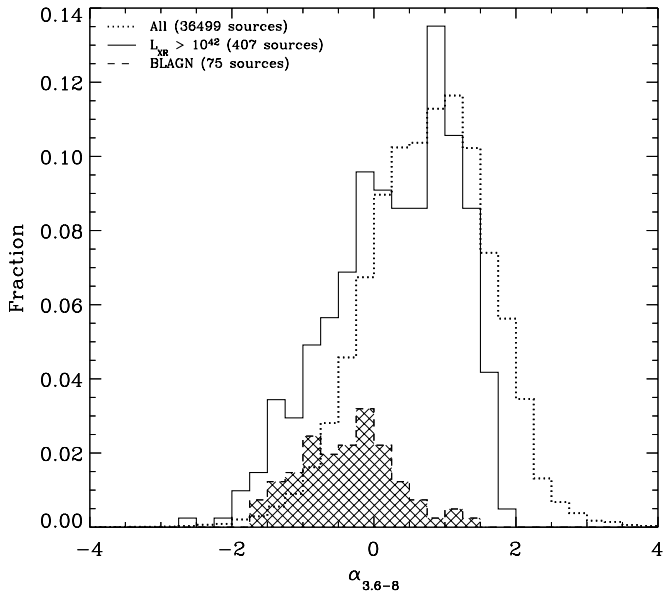

FIG. 3.—Histograms of the power-law index, α ($f_\nu \propto \nu^\alpha$), for fits to the *Spitzer* IRAC photometry. The X-ray sources with $L_X \geq 10^{42}$ ergs s^{-1} (*solid line*) and the subset of X-ray sources spectroscopically identified as BLAGNs (*cross-hatched histogram*) have been normalized to the total number of X-ray sources with good estimates of redshift and good power-law fits (396). Also plotted is the normalized histogram for all MUSYC sources well fit by power laws (38,988; *dotted line*). In total, 94% of all galaxies and 97% of the $L_X \geq 10^{42}$ ergs s^{-1} sources are consistent with a power-law SED. A K-S test rejects the hypothesis that these two distributions come from the same population ($P = 0.0014$). Although the AGNs are slightly redder than the galaxies, on average, both the AGNs and the galaxies are fit by a broad range of power-law slopes. [*See the electronic edition of the Journal for a color version of this figure.*]

(e.g., Lacy et al. 2004; Stern et al. 2005). Here, we examine what fraction of X-ray-selected AGNs would be selected using these techniques.

Lacy et al. (2004) found that a sample of Sloan Digital Sky Survey (SDSS) quasars occupied a distinct region of mid-infrared color-color space (Figs. 1 and 2). Because the selection box was defined using luminous type 1 quasars from SDSS, we look at the subset of the X-ray sources that have been identified as BLAGNs. Indeed, 96% of these sources fall inside the selected Lacy et al. region. Furthermore, all 61 X-ray sources identified photometrically as quasars in the COMBO-17 survey also fall inside this box. However, only 58% of all X-ray-selected AGNs fall inside this region. Thus, the percentage of X-ray-selected AGNs that lie inside this color selection box depends on the number of luminous type 1 objects in the sample. That is, this infrared color selection finds the luminous unobscured quasars but misses a high fraction of the lower luminosity AGNs, many of which look like optically normal galaxies. The brightest AGNs in our sample, $L_X \geq 10^{44.5}$ ergs s^{-1}, are also all located inside the Lacy et al. selection box. In addition, 18% of all sources (~11,000 galaxies) lie within the Lacy et al. selection box (Fig. 2). This is 20 times the total number of X-ray sources in this region (529). A reliable AGN selection criterion should yield a sample of sources containing mostly active galaxies. Because so many IRAC-detected sources fall inside this selection box, it is not a reliable method for selecting AGNs in deep surveys.

Stern et al. (2005) define a similar selection region using a deeper sample of spectroscopically confirmed AGNs from the Bootes field. In Figure 2 (*right*) we plot X-ray-selected sources on the Stern et al. (2005) color-color plot. Again, we find that the majority (76%) of our spectroscopically identified BLAGNs fall inside this selection box, but only 40% of X-ray-selected AGNs do. Over 90% of the brightest AGNs, $L_X \geq 10^{44.5}$ ergs s^{-1}, are

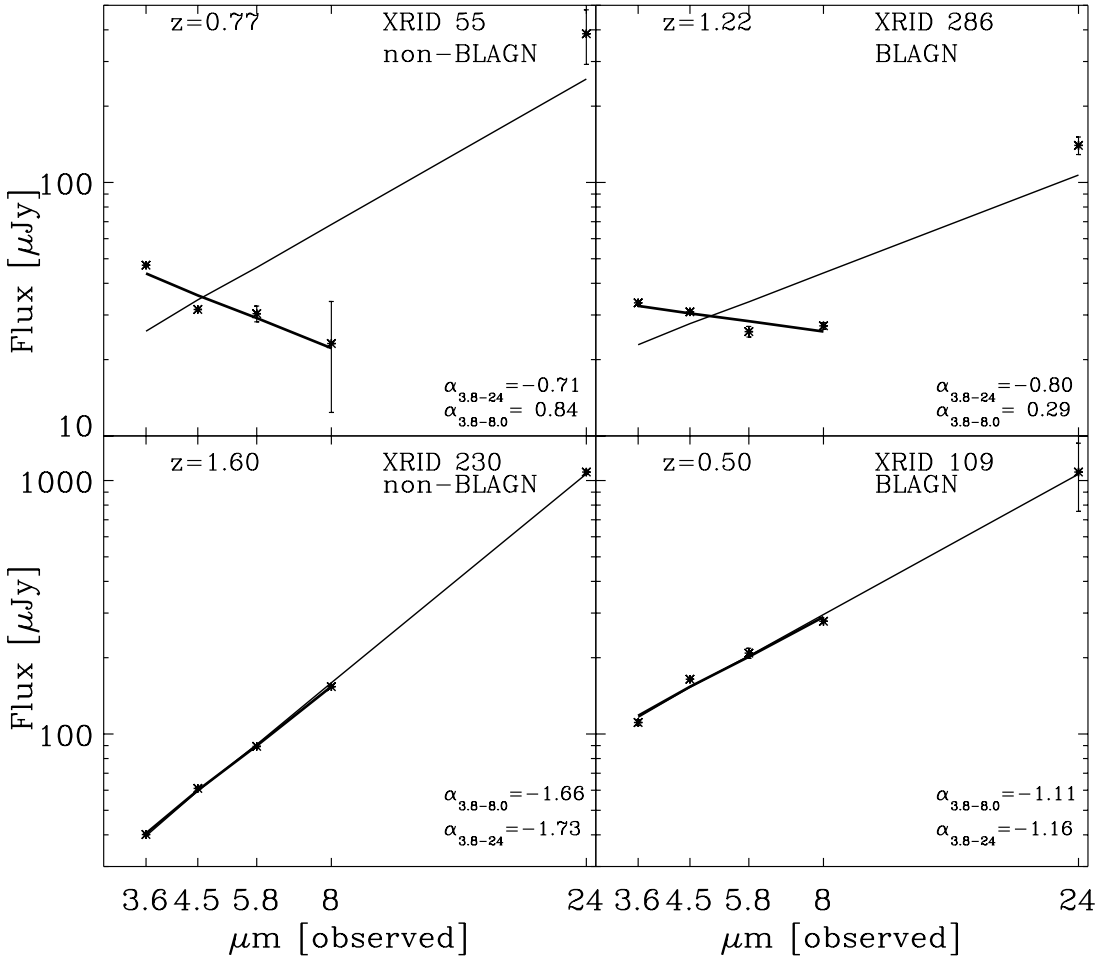

FIG. 4.—X-ray-selected AGNs show a variety of spectral shapes below 8 μm, but nearly all 24 μm–detected AGNs are very red between 3.6 and 24 μm. In the top panels, a power-law fit to 3.6–8 μm photometry is significantly bluer than a power-law fit including the 24 μm flux. In the bottom panels, the same power-law fits the 3.6–8 μm and the 3.6–24 μm data. Only ~25% of the MIPS sample falls into the latter category. The panels on the left are for sources identified spectroscopically as non-BLAGNs, while the panels on the right are BLAGNs. Thick lines show power-law fits to 3.6–8 μm and thin lines show fits including the 24 μm data point. [*See the electronic edition of the Journal for a color version of this figure.*]

also located inside the Stern selection box. In this case fewer galaxies lie inside this box (5163, ~8%), but they still outnumber the 340 X-ray sources by a factor of ~15. The Stern et al. (2005) selection criterion is a slightly more reliable way to select for candidate AGNs, but at the same time it misses a larger percentage of the total AGN population.

Although color selection techniques may work well for shallow surveys, where a larger percentage of the AGNs are bright and show broad lines, they are not as reliable in deep surveys. These selection boxes correctly highlight the region containing luminous broad-line quasars but miss most of the AGN population, in particular non-BLAGNs and low-luminosity AGNs. It is possible that some of the galaxies in these selection regions hide luminous AGNs. However, looking at Figure 2, there does not appear to be a clear region in color-color space that selects a complete sample of X-ray-detected AGNs and avoids returning a large portion of the entire galaxy population. In an effort to find a more reliable selection technique, we now add the 24 μm band data to our analysis of infrared colors.

4.1. 24 μm *Data*

Adding the 24 μm data to a given source's SED more than doubles the baseline over which we can determine the AGN spectral shape. For ~25% of our X-ray sources, consistent power-law fits are determined from the 3.6–8 μm and 3.6–24 μm data (e.g., Fig. 4, *bottom panels*). However, for many sources the best-fit power law to the IRAC data alone is much bluer than one that includes the 24 μm data (e.g., Fig. 4, *top panels*). We found a variety of spectroscopically identified BLAGNs and non-BLAGNs with 24 μm intensities that confirm the power-law slope from the IRAC data, as well as those whose 24 μm fluxes imply a distinct slope. In Figure 4 the sources on the left are identified as non-BLAGNs from optical spectra, while the sources on the right are BLAGNs. When adding the 24 μm flux to the fit, the median non-BLAGN slope changes from a value of $\alpha_{3.6-8\,\mu m} = 0.2$ to $\alpha_{3.6-24\,\mu m} = -1.0$, while the median BLAGN slope changes from a value of $\alpha_{3.6-8\,\mu m} = -0.3$ to $\alpha_{3.6-24\,\mu m} = -1.2$. The non-BLAGNs appear bluer on average in their 3.6–8.0 μm colors, while the BLAGNs are more likely to show a similar $\alpha_{3.6-8\,\mu m}$ and $\alpha_{3.6-24\,\mu m}$. While nearly all X-ray sources show a negative slope in their 3.6–24 μm spectrum, only for a minority (~25%) of X-ray sources is it a strictly monotonic rise.

In Figure 5 we directly compare the fitted index $\alpha_{3.6-8\,\mu m}$ with that of $\alpha_{3.6-24\,\mu m}$ for all 24 μm–detected sources. In this figure we include all sources whether or not their spectral shape is consistent with a power law. The X-ray-detected sources span a large range of $\alpha_{3.6-8\,\mu m}$, but in their longer wavelength color, $\alpha_{3.6-24\,\mu m}$, they are nearly uniformly red. In contrast, all galactic stars detected in X-rays and at 24 μm are in the upper left corner ($\alpha_{3.6-24\,\mu m} \geq 1$; *green symbols*). The histogram of $\alpha_{3.6-24\,\mu m}$ peaks below -1,

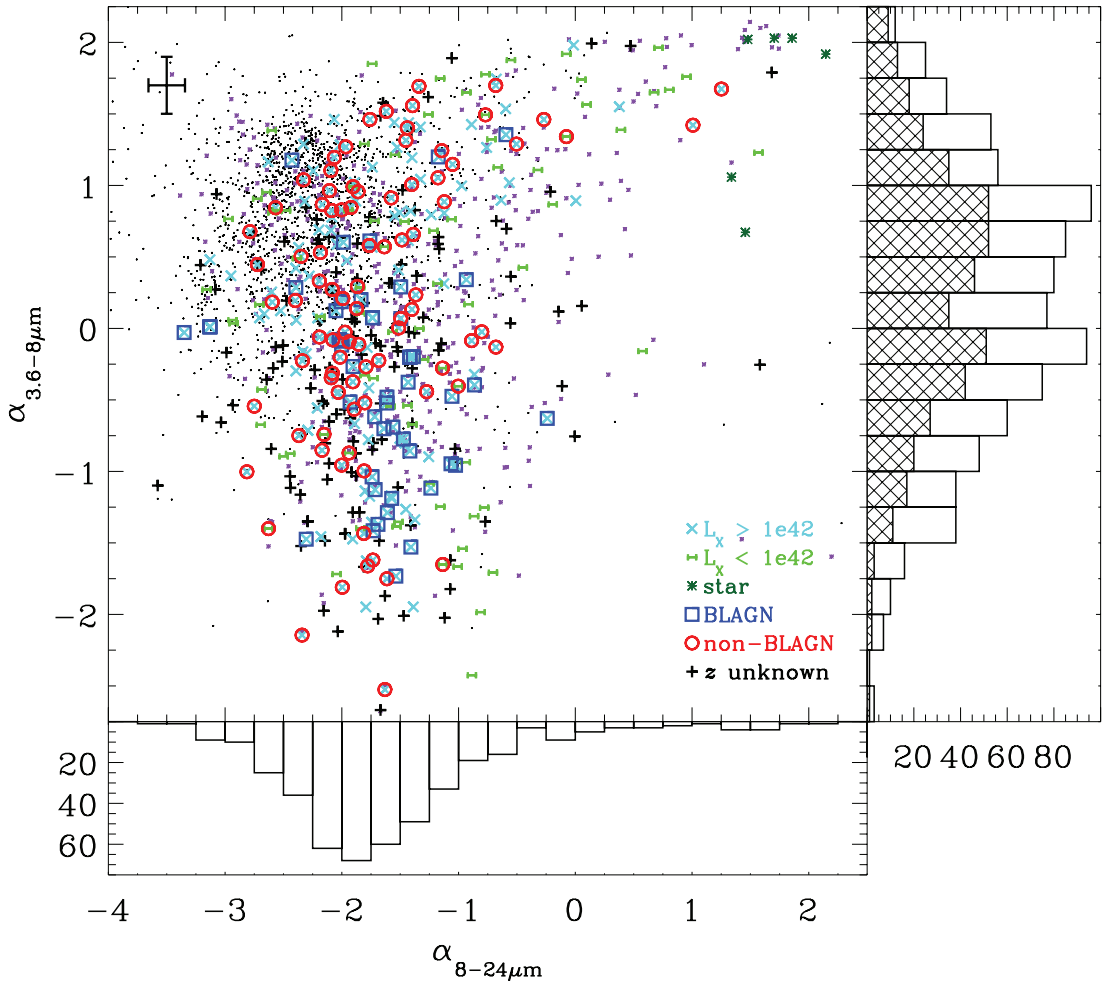

FIG. 5.—Comparison of the power-law slope ($f_\nu \propto \nu^\alpha$) from the IRAC bands, $\alpha_{3.6-8\ \mu m}$, to the power-law slope from all five bands between 3.6 and 24 μm. We include all sources whether or not $f_\nu \propto \nu^\alpha$ is a good fit to the data in order to study the approximate shape of the SED. For comparison we plot the GOODS sample of 24 μm–detected sources (*black symbols*) and indicate those that are consistent with a good power-law fit between 3.6 and 8 μm (*purple symbols*). The distribution of $\alpha_{3.6-24\ \mu m}$ equals peaks below -1.0 (*bottom panel*), significantly redder than either of the two peaks of the distribution of $\alpha_{3.6-8\ \mu m}$ for all sources (*right panel*). The cross-hatched histogram indicates sources lacking 24 μm detections. The deep GOODS data detect the 24 μm flux for sources with a large variety of IRAC spectral shapes. The median uncertainty in α for the X-ray sources is indicated in the top left corner. In the IRAC bands X-ray-selected AGNs show a wide range of colors, but beyond the observed 8 μm band, nearly all X-ray-selected AGNs fit very red spectral shapes, $\alpha \leq -1.0$. However, the 24 μm flux, which highlights cold dust, does not help separate AGNs from nonactive galaxies.

with ~90% of X-ray-selected AGNs detected at 24 μm having $\alpha_{3.6-24\ \mu m} \leq 0$ (Fig. 5, *bottom panel*). This histogram is quite different than that for the best-fit $\alpha_{3.6-8\ \mu m}$ (Fig. 5, *right panel*). The vast majority of X-ray sources with counterparts at 24 μm have $\alpha_{3.6-24\ \mu m} \leq 0$; we question whether this is because all AGNs have negative infrared slopes, or whether our shallow 24 μm coverage simply misses those AGNs that would show blue colors. We indicate sources without a 24 μm detection in the cross-hatched portion of the $\alpha_{3.6-8\ \mu m}$ histogram (Fig. 5, *right panel*). The deep GOODS data in the central portion return 24 μm magnitudes even for sources with very blue spectral shapes in the IRAC bands; we find no significant correlation between $\alpha_{3.6-8\ \mu m}$ and sources lacking 24 μm detections. Compared to 54% of all X-ray counterparts, 48% of the X-ray counterparts detected at 24 μm have blue spectral shapes below 8 μm ($\alpha_{3.6-8\ \mu m} \geq 0$). Only 20% of the X-ray-selected AGNs are consistent with a power-law SED from 3.6 to 24 μm (χ^2, $p \geq 0.05$), but of those that fit a power law, nearly all are negative power laws (34 out of 38 sources). This contrasts with only 43% of the X-ray-selected AGNs with IRAC power-law SEDs that have $\alpha_{3.6-8\ \mu m} \leq 0$. Although they have a large range in color below 8 μm, X-ray-selected AGNs detected at 24 μm are uniformly red beyond 8 μm. For comparison, we add all 24 μm–detected galaxies in GOODS to Figure 5 (*black symbols*) and indicate those that are consistent with a power-law SED between 3.6 and 24 μm (*purple symbols*). Many of these sources may be AGNs not detected at X-ray wavelengths, but the rest contain significant amounts of dust that is luminous at the observed 24 μm (Egami et al. 2004). The 24 μm data are not sufficient to differentiate the X-ray-selected AGNs from the non-X-ray-detected galaxies.

5. DISCUSSION

If the AGN contribution to an X-ray source SED is a red power law at infrared wavelengths, the infrared emission from most AGNs in the MUSYC sample must also include a significant contribution from the stars and dust in the host galaxy. Stellar spectra are declining in the infrared, creating a blue continuum for rest wavelengths $\lambda \geq 1.6$ μm. Because the peak of the redshift distribution for X-ray-selected AGNs in the ECDF-S is at $z \leq 1$, the AGN host galaxies will typically appear blue in the observed 3.6–8.0 μm band. For the lowest redshift objects, contributions from cool dust and PAH features can also contribute

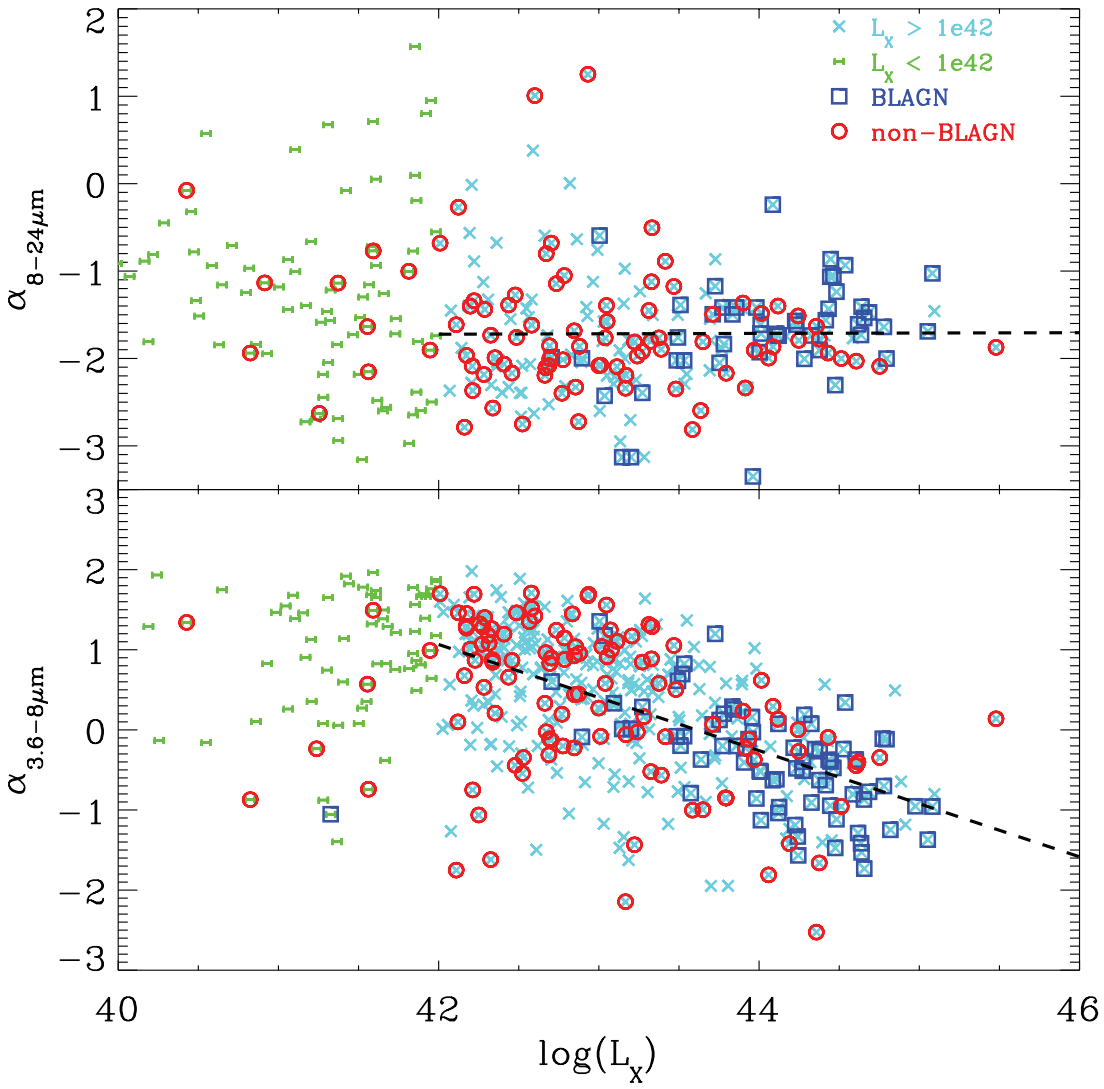

FIG. 6.—*Top*: At wavelengths longer than the observed 8 μm, there is no observed trend of $\alpha_{8-24\,\mu m}$ with X-ray luminosity. The slope of the best-fit line to the sources with $L_X \geq 10^{42}$ ergs s^{-1} is 0.04 ± 0.06 (*dashed line*). *Bottom*: More luminous X-ray sources have redder infrared power laws in the IRAC bands, $\alpha_{3.6-8\,\mu m}$, although in all cases there is a broad range. The slope of the best-fit line to the sources with $L_X \geq 10^{42}$ ergs s^{-1} is -0.6 ± 0.05 (*dashed line*). It is likely that the galaxy influence, which is proportionally larger for less luminous AGNs, is the origin of this trend.

to the observed mid-infrared light (Laurent et al. 2000). The 24 μm band is sensitive to dust emission in galaxies, making both AGNs and luminous star-forming galaxies easily detectable (Treister et al. 2006; Egami et al. 2004; Le Floc'h et al. 2004).

Figure 6 shows X-ray luminosity versus the fitted infrared power-law slope ($\alpha_{3.6-8\,\mu m}$, *bottom*; $\alpha_{8-24\,\mu m}$, *top*) for all MUSYC X-ray sources. Although there is a trend for brighter X-ray sources to have redder power laws below 8 μm, even some of the most luminous X-ray sources in the ECDF-S ($L_X = 10^{44}$–10^{45} ergs s^{-1}) have $\alpha_{3.6-8\,\mu m} \geq 0$. Because sources with similar L_X fit such a large range of $\alpha_{3.6-8\,\mu m}$, it is likely that varying contributions from the host galaxy (stars and cool dust) determine the different IRAC slopes. This is in agreement with the large number of non-BLAGNs that lie outside the infrared color selection box defined by optically selected quasars, and with what is seen in modestly obscured AGNs of Seyfert luminosities, where the host galaxy starlight can dominate the optical colors (Moran et al. 2002; Cardamone et al. 2007). In contrast, for infrared power-law-selected AGNs ($\alpha_{3.6-8\,\mu m} \leq 0$), the energetics are dominated by the central AGNs; thus, the signatures are often visible in the optical. Longward of 8 μm, there is no observed trend of spectral shape ($\alpha_{8-24\,\mu m}$) with X-ray luminosity. Our sample agrees with other studies that find that AGNs selected through IRAC power-law emission are the most luminous of those detected in X-rays (Donley et al. 2007) and with studies that look at the most luminous hard X-ray-detected AGNs and find them to have red mid-infrared colors (Georgantopoulos et al. 2007).

Supporting the idea that the colors below 8 μm are influenced by the host galaxy light is the fact that the X-ray spectral shape is entirely uncorrelated with the infrared spectral slope but correlated with optical AGN signatures. We plot $\alpha_{3.6-8\,\mu m}$ and $\alpha_{3.6-24\,\mu m}$ versus the X-ray hardness ratio, $(H - S)/(H + S)$, where H is the count rate in the hard band (2–8 keV) and S is the count rate in the soft band (0.5–2 keV), in Figure 7. The hardness ratio is set to -1 or $+1$ if the source is detected in only one of the two X-ray bands and is not shown here for detections only in the full band. The subset of sources with optical spectroscopy is indicated by squares (BLAGNs) and circles (non-BLAGNs), and sources consistent with power-law SEDs are also indicated (*asterisks*). There are fewer sources consistent with power-law spectral shapes between 3.6 and 24 μm, but there is no trend with X-ray hardness ratio. This result may indicate that the X-ray and infrared radiation

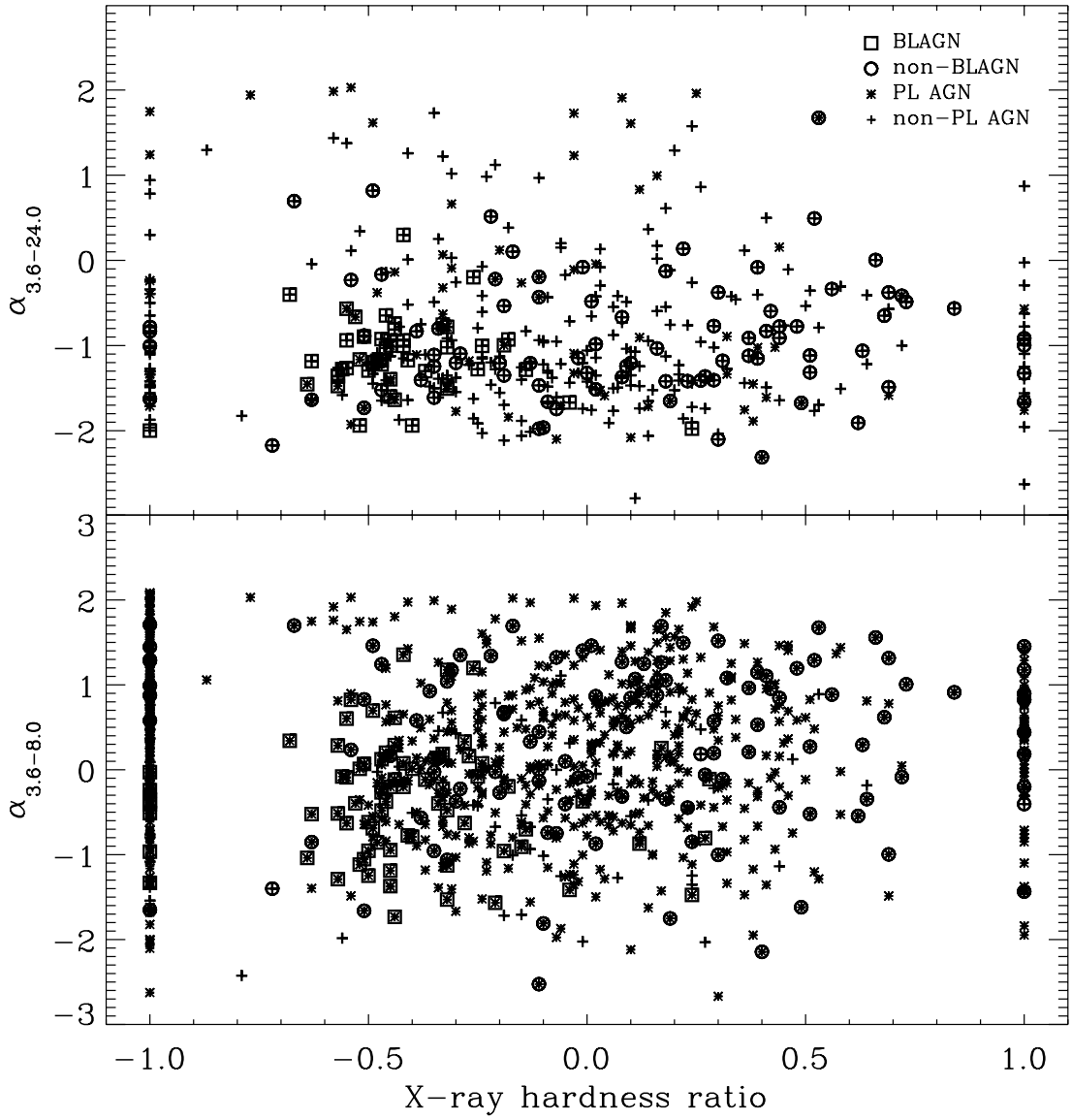

FIG. 7.—Power-law indices $\alpha_{3.6-24\,\mu m}$ (*top*) and $\alpha_{3.6-8\,\mu m}$ (*bottom*) vs. X-ray hardness ratio, $(H - S)/(H + S)$, where H represents the counts in the hard *Chandra* band (2–8 keV) and S represents the counts in the soft band (0.5–2 keV). Sources that are well fit by a power law over the given wavelength range (*asterisks*) are indicated; other sources (*crosses*) are plotted with a best-fit value of spectral slopes. The sequence of points at −1.0 (+1.0) are from sources detected only in the soft (hard) band. There is no correlation between observed slopes at X-ray and infrared wavelengths. The X-ray emission is most likely produced close to the black hole, while the mid-infrared emission likely comes from dust around the nucleus and in the host galaxy. [*See the electronic edition of the Journal for a color version of this figure*.]

is produced in vastly different environments. The X-rays produced near the central black hole are sensitive to obscuration near the central region, while the infrared reprocessed emission at wavelengths shorter than the observed 24 μm depends on the dust distribution not only around the nucleus but throughout the galaxy. In contrast, the optical identifications based on emission lines are somewhat correlated with hardness ratio: the left side of Figure 7, i.e., negative X-ray hardness ratios (relatively soft spectra), is preferentially occupied by BLAGNs. This reinforces the idea that the observed infrared emission is insensitive to the geometry, or more likely, includes a substantial contribution from the host galaxy itself.

Our results are consistent with the findings for other X-ray-selected samples, where a significant fraction of the X-ray-detected AGNs have bluer colors indistinguishable from those of galaxies (e.g., Franceschini et al. 2005; Barmby et al. 2006). Treister et al. (2006) concluded that a fair fraction of the mid-infrared light in low-luminosity AGNs arises from the host galaxies, based on the large overlap in the infrared luminosity distributions of normal galaxies and lower luminosity AGNs in the GOODS sample. Hickox et al. (2007) showed that sources were moved into mid-infrared selection boxes by combining an AGN template with increasing strength with a galaxy template. Mid-infrared selection techniques can miss a significant fraction of AGNs if the high column densities significantly dim the central power-law emission and/or starlight significantly dilutes the AGN continuum.

Mid-infrared selection techniques can uncover sources whose SEDs are dominated by the central AGN emission. AGNs undetected in *Chandra* or *XMM-Newton* surveys because of heavy obscuration are very likely to be bright infrared sources. Alonso-Herrero et al. (2006) used the 24 μm–detected sample of sources in GOODS-South to select IRAC power-law galaxies. Only half of their sample was individually detected at X-ray wavelengths. Polletta et al. (2006) effectively used infrared color selection

techniques to uncover a sample of heavily obscured quasars. Their selection was based on featureless SEDs, and they deliberately removed any source that could be fit acceptably by a galaxy spectral template. A complementary study by Daddi et al. (2007) examined non-X-ray-detected galaxies, which were not dominated by power-law continuum emission in the IRAC bands, and uncovered a detectable contribution from hot dust near an AGN in 20%–30% of the sample. This emission was discovered in excess mid-infrared flux above and beyond the amount predicted from star formation indicators at other wavelengths. These galaxies lack any detectable signatures of AGN emission at optical wavelengths, but stacking results at X-ray wavelengths point toward obscured AGN emission (Daddi et al. 2007).

A well-defined subset of the X-ray counterparts detected at all infrared wavelengths is well-fit by red (negative) power laws from 3.6 to 24 μm. These sources have similar red power laws ($\alpha \leq 0$), lie inside the standard infrared selection boxes for optically selected AGNs, and show preferentially broad lines in their optical spectra. About 25% of the whole sample fits into this category. This is an upper bound, since the shallow 24 μm coverage in SWIRE may bias us toward redder X-ray sources. To check this, we selected a sample of sources in the deeper GOODS area that are bright enough at 3.6 μm to be detected at 24 μm, even if they have a blue slope ($\alpha = +1$). Of these 26 X-ray sources with bright 3.6 μm magnitudes ($m_{3.6} \leq 21.4$), 4 have a monotonic red slope between 3.6 and 24 μm. This is a slightly lower fraction (15%) but consistent within the statistics with the 25% seen in the large sample. These mid-infared power-law sources tend to be the most luminous X-ray sources. Together with their Compton-thick counterparts undetected at X-ray wavelengths, these are the best candidates for infrared selection techniques.

6. CONCLUSIONS AND SUMMARY

AGNs are luminous infrared sources, and deep infrared data from *Spitzer* potentially provide powerful new methods for selecting AGN samples. In this paper, we examined the infrared properties of a large sample of AGNs at moderately high redshifts selected through their X-ray emission. In the observed 3.6–8.0 μm band, over half of these X-ray-selected AGNs show infrared colors consistent with those of galaxies. Across the narrow wavelength range of the IRAC filters, most galaxies are also consistent with power-law spectral shapes. As a result, IRAC data alone are not sufficient for a complete or reliable selection of (moderate-luminosity) AGNs. At 24 μm, dust from both star-forming galaxies and AGNs is detected. Unfortunately, observed IRAC to 24 μm colors do not effectively separate galaxies powered by AGNs from those experiencing star formation. Previous studies with *IRAS* have shown the far-infrared to be valuable for discriminating active from inactive galaxies (Sanders & Mirabel 1996); to apply similar techniques to present deep surveys requires longer wavelength data, not just at 24 μm but at 70 μm and, if possible, 160 μm as well.

To develop complete samples of AGNs, we need to understand what kinds of AGNs each selection criterion returns. Infrared selection returns a slightly different population than X-ray selection. Future studies using complete SEDs from the ultraviolet through infrared will help disentangle the contribution from the central AGN from that of the host galaxy. We have imaged the entire ECDF-S with medium-band filters, which will result in high-quality photometric redshifts for most of the AGNs and will allow us to disentangle the nuclear and host galaxy light. These data will also reveal the origin of the variety of infrared colors shown below 8 μm. The large range in color shown by AGNs below 8 μm potentially holds valuable information about the star formation processes going on in the AGN host galaxies and may help us understand the AGN-galaxy connection.

We thank the anonymous referee for constructive comments that improved this paper. Support from NSF grant AST 04-07295 and *Spitzer* JPL grant RSA1288440 is gratefully acknowledged.

REFERENCES

Alexander, D. M., et al. 2003, AJ, 126, 539 (A03)
Alonso-Herrero, A., et al. 2006, ApJ, 640, 167
Barmby, P., et al. 2006, ApJ, 642, 126
Bertin, E., & Arnouts, S. 1996, A&AS, 117, 393
Brandt, W. N., & Hasinger, G. 2005, ARA&A, 43, 827
Brinkmann, W., Laurent-Muehleisen, S. A., Voges, W., Siebert, J., Becker, R. H., Brotherton, M. S., White, R. L., & Gregg, M. D. 2000, A&A, 356, 445
Brusa, M., et al. 2005, A&A, 432, 69
———. 2007, ApJS, 172, 353
Cardamone, C. N., Moran, E. C., & Kay, L. E. 2007, AJ, 134, 1263
Ciliegi, P., Vignali, C., Comastri, A., Fiore, F., La Franca, F., & Perola, G. C. 2003, MNRAS, 342, 575
Croom, S. M., Warren, S. J., & Glazebrook, K. 2001, MNRAS, 328, 150
Croton, D. J., et al. 2006, MNRAS, 365, 11
Daddi, E., et al. 2007, ApJ, 670, 173
Dickinson, M., et al. 2003, in The Mass of Galaxies at Low and High Redshift, ed. R. Bender & A. Renzini (Berlin: Springer), 324
Donley, J. L., Rieke, G. H., Pérez-González, P. G., Rigby, J. R., & Alonso-Herrero, A. 2007, ApJ, 660, 167
Dwelly, T., & Page, M. J. 2006, MNRAS, 372, 1755
Egami, E., et al. 2004, ApJS, 154, 130
Elvis, M., et al. 1994, ApJS, 95, 1
Fabian, A. C., Sanders, J. S., Allen, S. W., Crawford, C. S., Iwasawa, K., Johnstone, R. M., Schmidt, R. W., & Taylor, G. B. 2003, MNRAS, 344, L43
Fabian, A. C., Sanders, J. S., Taylor, G. B., Allen, S. W., Crawford, C. S., Johnstone, R. M., & Iwasawa, K. 2006, MNRAS, 366, 417
Fazio, G., et al. 2004, ApJS, 154, 10
Franceschini, A., et al. 2005, AJ, 129, 2074
Freeman, P. E., Kashyap, V., Rosner, R., & Lamb, D. Q. 2002, ApJS, 138, 185
Gawiser, E., et al. 2006, ApJS, 162, 1
Georgantopoulos, I., Georgakakis, A., & Akylas, A. 2007, A&A, 466, 823
Giacconi, R., et al. 2002, ApJS, 139, 369 (G02)
Granato, G. L., & Danese, L. 1994, MNRAS, 268, 235
Hatziminaoglou, E., et al. 2005, AJ, 129, 1198
Hickox, R. C., et al. 2007, ApJ, 671, 1365
Kriek, M., et al. 2007, ApJ, 669, 776
Lacy, M., et al. 2004, ApJS, 154, 166
Laurent, O., Mirabel, I. F., Charmandaris, V., Gallais, P., Madden, S. C., Sauvage, M., Vigroux, L., & Cesarsky, C. 2000, A&A, 359, 887
Le Fèvre, O., et al. 2004, A&A, 428, 1043
Le Floc'h, E., et al. 2004, ApJS, 154, 170
Lehmer, B. D., et al. 2005, ApJS, 161, 21 (L05)
Lira, P., Ward, M., Zezas, A., Alonso-Herrero, A., & Ueno, S. 2002, MNRAS, 330, 259
Lonsdale, C. J., et al. 2003, PASP, 115, 897
Mazzarella, J. M., & Balzano, V. A. 1986, ApJS, 62, 751
Moran, E. C., Filippenko, A. V., & Chornock, R. 2002, ApJ, 579, L71
Mukai, K. 1993, Legacy, 3, 21
Nenkova, M., Ivezić, Ž., & Elitzur, M. 2002, ApJ, 570, L9
Persic, M., et al. 2004, A&A, 427, 35
Pier, E. A., & Krolik, J. H. 1992, ApJ, 401, 99
Polletta, M. d. C., et al. 2006, ApJ, 642, 673
Quadri, R., et al. 2007, AJ, 134, 1103
Richards, G. T., et al. 2004, ApJS, 155, 257
———. 2006, ApJS, 166, 470
Rieke, G., et al. 2004, ApJS, 154, 25
Sanders, D. B. 1999, in IAU Symp. 194, Activity in Galaxies and Related Phenomena, ed. Y. Terzian, E. Khachikian, & D. Weedman (San Francisco: ASP), 25
Sanders, D. B., & Mirabel, I. F. 1996, ARA&A, 34, 749

Sanders, D. B., Phinney, E. S., Neugebauer, G., Soifer, B. T., & Matthews, K. 1989, ApJ, 347, 29
Schawinski, K., Thomas, D., Sarzi, M., Maraston, C., Kaviraj, S., Joo, S.-J., Yi, S. K., & Silk, J. 2007, MNRAS, 382, 1415
Severgnini, P., et al. 2003, A&A, 406, 483
Sijacki, D., Springel, V., di Matteo, T., & Hernquist, L. 2007, MNRAS, 380, 877
Stern, D., et al. 2005, ApJ, 631, 163
Streblyanska, A., Bergeron, J., Brunner, H., Finoguenov, A., Hasinger, G., & Mainieri, V. 2004, Nucl. Phys. B Proc. Suppl., 132, 232
———. 2006, in IAU Symp. 230, Populations of High Energy Sources in Galaxies, ed. E. J. A. Meurs & G. Fabbiano (San Francisco: ASP), 450
Surace, J. A., et al. 2005, BAAS, 37, 1246
Sutherland, W., & Saunders, W. 1992, MNRAS, 259, 413
Szokoly, G. P., et al. 2004, ApJS, 155, 271
Treister, E., & Urry, C. M. 2006, ApJ, 652, L79
Treister, E., et al. 2004, ApJ, 616, 123
———. 2006, ApJ, 640, 603
Vanzella, E., et al. 2005, A&A, 434, 53
Virani, S. N., Treister, E., Urry, C. M., & Gawiser, E. 2006, AJ, 131, 2373 (V06)
Wolf, C., et al. 2004, A&A, 421, 913
Worsley, M. A., et al. 2005, MNRAS, 357, 1281